Title: Reversible fusion and fission of graphene oxide based fibers

Authors: Dan Chang[1], Jingran Liu[2], Bo Fang[1], Zhen Xu[1], Zheng Li[1]*, Yilun Liu[2]*, Laurence Brassart[3], Fan Guo[1], Weiwei Gao[1] & Chao Gao[1]*

Affiliations:

[1]MOE Key Laboratory of Macromolecular Synthesis and Functionalization, Department of Polymer Science and Engineering, Key Laboratory of Adsorption and Separation Materials & Technologies of Zhejiang Province, Zhejiang University, 38 Zheda Road, Hangzhou 310027, China.

[2]State Key Laboratory for Strength and Vibration of Mechanical Structures, School of Aerospace, Xi'an Jiaotong University, Xi'an 710049, China.

[3]Department of Materials Science and Engineering, Monash University, Clayton Victoria 3800, Australia. Now at Department of Engineering Science, University of Oxford, Oxford OX1 3PJ, United Kingdom.

*Corresponding author. Email: lizheng_zju@zju.edu.cn (Z.L.); yilunliu@mail.xjtu.edu.cn (Y.L.); chaogao@zju.edu.cn (C.G.)

Abstract:

Stimuli-responsive fusion and fission are widely observed in both bio-organizations and artificial molecular assemblies. However, the design of a system with structure and property persistence during repeated fusion and fission remains challenging. We show reversible fusion and fission of wet-spun graphene oxide (GO) fibers, where numbers of macroscopic fibers can

fuse into a thicker one, and can also separate into original individual fibers under stimulation of solvents. The dynamic geometrical deformation of GO fiber shells, caused by solvent evaporation and infiltration, is the key to the reversible fusion-fission cycles. This principle is extended to implement flexible transitions between complex fiber assemblies and the inclusion or expulsion of guest compounds.

One Sentence Summary:

Large geometrical deformation of macroscopic fibers enables reversible fusion and fission under solvent stimuli.

Main Text:

Fusion and fission behaviors have been extensively studied in biology, chemical engineering and theoretical physics to understand cellular processes, develop morphological events of artificial assemblies and create multimetallic compounds. Fusion and fission of lipid/surfactant/small organic molecules/polymer micelles and vesicles are usually triggered by either introducing salts, surfactants, ions, and oxidant/reductant or applying UV and visible light to change the interactions inside bilayer membranes, as well as by dissolving additives such as saccharides to alter the osmotic pressure between the aqueous interior of vesicles and the bulk solution (*1*-*6*). Similar behaviors of metal particles/clusters are also induced by heat or cluster deposition (*7*-*9*). Although progress has been made on fusion-fission of artificial vesicles and nanoparticles, reversible fusion and fission are still difficult to realize, mainly because of the irreversible physical or chemical changes at the interface between individual assemblies. The exploration of reversible and controllable fusion and fission would inspire the development of stimuli-responsive materials, which show promise in deriving dynamic transformable systems

and structural materials with customized fibrous substructures. The recyclability of the assembled structures is also a beneficial attribute.

We propose a solvent-triggered topography-regulation strategy to implement reversible fusion and fission. GO fiber is selected as a model owing to the nature of GO sheets including 2D topology, abundant chemical moieties, super-flexibility and self-adhesion capability (*10-13*). After swelling (*14*), the wet-spun GO fiber features a shell (an outermost skin) that confines the movement of internal GO sheets and shows a solvent-triggered large volume change and elastic deformation capability. Upon stimuli of water and polar organic solvents, the topography of fiber shells reversibly switches between a wrinkled, tubular state and a spread cylindrical state via swelling and deswelling thus causing a transient fiber interface and leading to cyclic self-fusion and self-fission of an arbitrary number of GO fibers (Fig. 1A). In each cycle, the number, size, composition, structure and property of GO fibers are recovered after fission, exhibiting the precise reversibility of fusion and fission.

Continuous GO fibers were prepared following a wet-spinning protocol (fig. S1) (*15, 16*). In Fig. 1B, we demonstrate the reversible fusion and fission involving up to 100 GO fibers (movie S1). For simplicity, the fused GO fiber assembled by *n* individual fibers is denoted as FuF-*n*, and the corresponding fissured individual dried GO fiber is denoted as FiF-*n*. A typical fusion process requires three steps, including solvent-swelling of fibers in a bundle, drawing the fiber bundle out of the solvent, and air-drying. The fission steps comprise reswelling of the fused fiber in a solvent, splitting of swelled fiber bundles, and drying of the fissured fibers separately (see supplementary materials).

In situ optical microscopy and ex situ scanning electron microscopy (SEM) show the water-induced fusion and fission processes (Fig. 1, C to F, figs. S2 and S3, and movies S2 and S3).

Swelling ratio, defined as the ratio of swelled fiber diameter to raw fiber diameter, is employed to quantify the extent of swelling which is influenced by solvent type, chemical nature of GO fibers as well as the soaking time (fig. S4) (*17*). The equilibrium-swelled GO fibers randomly immersed in water exhibit a swelling ratio of 541% with a core-shell structure, where the core (pore size of 2-5 μm after freeze-drying, inner wall thickness of 28 ± 8 nm) is enclosed by a skin-like shell (about 80 ± 18 nm-thick) of densely packed GO sheets that orient along the circumference (Fig. 1C1 and D1, and figs. S5 and S6). This different arrangement of GO sheets within the outer layer and inner fiber is a featured structure of wet-spun fibers, which originates from the aligning effect during fiber extrusion, and is enhanced by double diffusive convection in the coagulation bath (*18*). The thickness of both shell and inner wall depends on the swelling of fibers that relates to the quantity of absorbed solvent. Driven by the surface tension of water, these swelled fibers collect together and deform into a cylindrical group spontaneously as they are drawn out from the liquid. During air-drying (0-40 min), the swelled fibers bond together accompanied with adaptive crumpling of fiber shells exhibiting a volume shrinkage of 98% (Fig. 1, C1 to C4 and D1 to D4). Meanwhile, the interlayer spacing decreases from above 2.21 nm to 0.84 nm according to in-situ X-ray diffraction (XRD) characterizations (fig. S7A). Consequently (40 min), the resulted FuF-100 features compact packing of GO platelets (interlayer spacing of 0.84 nm, density of 1.51 g cm^{-3}) with a tensile strength of 281 MPa (fig. S2, G to I). GO fibers also fuse while drying not under tension, despite the decrease in density and tensile strength compared with those drying under tension (fig. S8).

Fission of FuF-100 starts with a homogeneous swelling when it is re-soaked in water, and small gaps emerge at the inter-fiber interfaces as the swelling persists. Subsequently (150 s), a rapid gap propagation, along with volume expansion of the whole fiber assembly leads to the

complete fission into 100 individual quasi-cylindrical fibers. The fissured fibers sustain in water for a long time rather than dissolving into pieces despite a swelling ratio of 538 %, also owing to the protective effect of the outer shell. During the whole process, solvent infiltration causes expansion between GO sheets, with interlayer spacing restoring from 0.84 nm to above 2.21 nm (fig. S7B). After drying separately, the interlayer spacing between GO sheets (0.84 nm), density (1.54 g cm^{-3}) and tensile strength (259 MPa) of FiFs-100 are close to those of FuF-100 (fig. S2). In-situ optical microscopy/polarized optical microscopy observations on the cross-section of two GO fibers during their fusion and fission further verify the above description (movie S3).

A GO fiber was labelled with fluorescent 1, 1, 2-triphenyl-2-(4-bromomethylphenyl) ethylene (TPE-Br) and silicon (Si) nanoparticles. Tracking on the fusion and fission of the labelled fiber and a pristine one under fluorescence microscope reveals no substance exchange across the fiber interface (Fig. 2, A to D, fig. S9 and movie S4). Energy dispersive spectroscopy (EDS) analysis performed on a neat GO fiber and another composite Si/GO fiber (Fig. 2, E to L, and figs. S10 and S11) shows that fusion was finally accomplished by interlocking of the synergistically crumpled shells, and fission was induced by topographical recovery of shells with opposite normal vectors in geometry on both sides of the bonding interface (Fig. 2K, L).

On the basis of the above characterizations, fusion and fission were found to be conducted by reversible crumpling and spreading of fiber shells while deswelling and reswelling (Fig. 3A, and figs. S12 and S13). Here the GO fiber shell is defined as the outermost dense layer of a saturated swelled GO fiber, characterized by macro-scale cylindrical configuration, micro-scale ripples and nanoscale closely organized GO platelets (fig. S13). The shell plays a major role in the reversible fusion-fission process because it is the boundary contacting with adjacent fibers, which provides inter-fiber bonding/debonding and protects inner-fiber GO sheets from diffusion.

A swelled GO fiber almost maintains a constant perimeter during deswelling and reswelling courses, indicating only elastic deformation occurs at the shell (Fig. 3B). The shell crumples and spreads due to wrinkling and unfolding of the ripple microstructures, with the curvature radius of the ripples varies in the range of about 10 nm to 83 μm (Fig. 3C, and fig. S13, A1 to B4). At the same time, the inner-fiber GO sheets deform accordingly since they are interconnected in the swelled gel fiber. Notably, the reversible fusion-fission capability is only found in wet-spun GO fibers. Although dry-spun GO fibers can be fused, they failed to fissure, mainly attributed to the insufficiency of a dense and protective shell (fig. S14) (*19*). The topographical and volumetric evolution of fibers during fusion process is driven by the surface tension of solvent (*20*) and the Laplace pressure difference (P_c) (*21*). The attractive stress P_c facilitates further bonding of fiber shells via non-covalent interactions (π-π interaction and hydrogen bonding (*22*)), as well as subsequent wrinkling of GO sheets and densifying of the whole fiber bundle (fig. S15A). During the fusion process, the solvent-responsive fiber shell acts as an elastic barrier, preventing the sheet interdiffusion across the transient interface. Herein, the fusion degree, proposed to evaluate the fusion status (see supplementary materials for calculation), rises from 0% (unfused) to 100% (fused) upon swelling and traverses a hemifused region (swelling ratio from 165% to 358%) (fig. S16).

Conversely, fission is attributed to the cylindrical geometry-driven detachment between fiber shells (fig. S17A). As the FuF is soaked in good solvents for GO, the solvent infiltration weakens the adhesion strength (σ_{ad}*) between individual fibers (*23*). The tendency of cylindrical geometry reversion at the interface contributes to the interfacial detachability and compels the attached fibers to separate from each other. This repulsion is estimated by the net stress (denoted as fission stress σ_{fis}) of elastic tensile stress σ_{e1} and swelling pressure p_s along the inward-

pointing normal direction of the curved microelement (see supplementary materials). This hypothesis is further confirmed by finite element analysis, which shows σ_{fis} is generated by the curved geometry of shell when the swelling ratio of individual fibers surpasses a sufficiently high value (475% and 521 % for separation of point 1 and 2, respectively) (fig. S17, B to E and movie S5). Further swelling leads to the rising σ_{fis}, which consequently reaches a peak value equal to σ_{ad}* and triggers a sudden drop of σ_{fis} to 0 MPa. In fission experiments, the fission capability of FuF-2 was initiated when the average swelling ratio of individual fibers traverses a critical range from 310% to 419%, either by applying polarity-enhanced solvent or reducing the pre-treating temperature on the FuF-2 (fig. S18A). Additionally, in contrast to GO fibers, GO belts featuring a distinct flat topography after swelling are able to be fused together but fail to fissure, due to the absence of an arc conformation of GO sheets stored in wrinkles thus lacking a driving force σ_{fis} for self-fission (fig. S19).

The morphology and structure of both FiF-50 and FuF-50 are recovered throughout multiple fusion-fission cycles, while exhibiting a relatively constant tensile strength of 281 MPa and 259 MPa, respectively (Fig. 3D, fig. S20 and movie S6). After several cycles, the interlayer spacing of GO sheets in fibers remains unchanged at the same fusion or fission time (fig. S21). Additionally, there is no apparent decline in the tensile and compressive strength of FuFs when the fiber diameter increases from 23 to 78 μm (by increasing the number of individual GO fibers engaged in fusion from 10 to 100) (fig. S22). The values are stable at about 282 and 129 MPa, respectively. After thermal reduction at 1000 ℃, the FuF-100 exhibits a tensile strength of 597 MPa with a diameter of 58 μm. The consistency of the mechanical performances reflects that the stacking order within individual GO fibers remains intact. One advantage of thick FuFs is the firmly combined fibers are stronger than either the as-spun thick GO fibers or the unfused yarns

with separated fibers (figs. S22B and S2I). Therefore the affordable force on the thick FuFs is higher, better for structural materials which may exert mechanical superiority in engineering fields. Fluorescence tracking and EDS analysis on the labelled GO fibers further showed the cycles of reversible fusion and fission (figs. S23 and S24). Investigation on bundles composed of one Si/GO fiber and 99 neat GO fibers shows that the relative atomic content of Si in the Si/GO fiber remains constant whether the Si-labelled fiber is within the fused fiber surrounded by neat GO fibers or at the fissured state (fig. S24, C to E; see supplementary materials for calculation).

Fig. 4 demonstrates concepts for potential application of the fusion-fission behavior. First, flexible transformation between diverse fiber-based assembled structures becomes possible. This would allow adaptive application of GO fiber-based systems in different scenarios with specific performance needs. For instance, the GO fiber assemblies are demonstrated to transform reversibly between a 3D stiff rod and a 2D flexible net via fission and re-fusion (Fig. 4, A to D, fig. S25A, and movie S7). In this case, as many as 13,500 fibers with micrometer-scale diameter and centimeter-scale length were fused into one 1.2 mm-thick rod that is rigid and strong enough to support 680 times its weight. Alternatively, transitions between a 1D fused GO fiber and various 1D and 2D sophisticated fiber assemblies were also conducted by localized fission and fusion (Fig. 4E, F, and movie S8). The second possible application is that, through fusion and fission, a GO fiber bundle would be able to implement functions of including and expelling of guest objects, which may show promise in dynamic systems for controllable delivery. Various guest objects of different material, size and shape, for instance, polyacrylonitrile chopped fibers, polystyrene microspheres, and glass beads in sub-millimeter scale were absorbed into a FuF during fusion and then expelled during fission (Fig. 4, G to J, fig. S26, and movie S9). The third application is endowing ordinary fibers with reversible fusion and fission property through GO

coating. Conventional polymer, metal and ceramic fibers were endowed with the reversible fusion-fission capability by simply coating a GO outer layer (figs. S27 and S28, and movie S10). This extension further expands the coverage of corresponding application fields.

Precisely reversible fusion and fission were induced here by the recoverable geometrical deformation of GO fibers. This enabled a dynamic feature in the fiber-assembled system so that transformation among structures and responsive actuation was realized. The concept was further expanded to conventional fibers through GO coatings, while providing the potential for recyclability. The featured fusion-fission behavior constitutes a versatile strategy for the design of functional responsive materials.

References and Notes:

1. F. Menger, N. Balachander, Chemically-induced aggregation, budding, and fusion in giant vesicles: direct observation by light microscopy. *J. Am. Chem. Soc.* **114**, 5862-5863 (1992).
2. Y. Zhou, D. Yan, Real-time membrane fusion of giant polymer vesicles. *J. Am. Chem. Soc.* **127**, 10468-10469 (2005).
3. Y. Zhou, D. Yan, Real-time membrane fission of giant polymer vesicles. *Angew. Chem. Int. Ed.* **44**, 3223-3226 (2005).
4. J. C. Shillcock, R. Lipowsky, Tension-induced fusion of bilayer membranes and vesicles. *Nat. Mater.* **4**, 225-228 (2005).
5. H. Cai, G. Jiang, Z. Shen, X. Fan, Solvent-induced hierarchical self-assembly of amphiphilic PEG(G_m)-*b*-PS dendritic-linear block copolymers. *Soft Matter* **9**, 11398-11404 (2013).
6. Y. Rharbi, M. Karrouch, P. Richardson, Fusion and fission inhibited by the same mechanism in electrostatically charged surfactant micelles. *Langmuir* **30**, 7947-7952 (2014).
7. Y. Yao *et al.*, Carbothermal shock synthesis of high-entropy-alloy nanoparticles. *Science* **359**, 1489-1494 (2018).
8. P. Jensen, Growth of nanostructures by cluster deposition: experiments and simple models. *Rev. Mod. Phys.* **71**, 1695-1735 (1999).
9. C. C. Wang *et al.*, Ultrafast shape change and joining of small-volume materials using nanoscale electrical discharge. *Nano Res.* **8**, 2143-2151 (2015).
10. J. Kim, L. J. Cote, J. X. Huang, Two dimensional soft material: new faces of graphene

oxide. *Accounts Chem. Res.* **45**, 1356-1364 (2012).

11. S. Presolski, M. Pumera, Graphene oxide: carbocatalyst or reagent? *Angew. Chem. Int. Ed.* **57**, 16713-16715 (2018).

12. P. Poulin *et al.*, Superflexibility of graphene oxide. *Proc. Natl Acad. Sci.* **113**, 11088-11093 (2016).

13. C. Luo, C. N. Yeh, J. M. L. Baltazar, C. L. Tsai, J. Huang, A cut-and-paste approach to 3D graphene-oxide-based architectures. *Adv. Mater.* **30**, 1706229 (2018).

14. Z. Li, Z. Xu, Y. J. Liu, R. Wang, C. Gao, Multifunctional non-woven fabrics of interfused graphene fibres. *Nat. Commun.* **7**, 11 (2016).

15. Z. Xu, C. Gao, Graphene chiral liquid crystals and macroscopic assembled fibres. *Nat. Commun.* **2**, 571 (2011).

16. B. Fang, D. Chang, Z. Xu, C. Gao, A review on graphene fibers: expectations, advances, and prospects. *Adv. Mater.* **29**, 1902664 (2019).

17. M. Tanaka *et al.*, Wetting and dewetting of extracellular matrix and glycocalix models. *J. Phys.-Condens. Mat.* **17**, S649 (2005).

18. Z. Xu, C. Gao, Graphene in macroscopic order: liquid crystals and wet-spun fibers. *Accounts Chem. Res.* **47**, 1267-1276 (2014).

19. Q. Tian et al., Dry spinning approach to continuous graphene fibers with high toughness. *Nanoscale* **9**, 12335-12342 (2017).

20. X. Li *et al.*, Directly drawing self-assembled, porous, and monolithic graphene fiber from chemical vapor deposition grown graphene film and its electrochemical properties. *Langmuir* **27**, 12164-12171 (2011).

21. D. Chandra, S. Yang, Stability of high-aspect-ratio micropillar arrays against adhesive

and capillary forces. *Accounts Chem. Res.* **43**, 1080-1091 (2010).

22. H. Cheng *et al.*, Self-healing graphene oxide based functional architectures triggered by moisture. *Adv. Funct. Mater.* **27**, 1703096 (2017).

23. N. V. Medhekar, A. Ramasubramaniam, R. S. Ruoff, V. B. Shenoy, Hydrogen bond networks in graphene oxide composite paper: structure and mechanical properties. *ACS Nano* **4**, 2300-2306 (2010).

24. X. L. Zhao *et al.*, Ion diffusion-directed assembly approach to ultrafast coating of graphene oxide thick multilayers. *ACS Nano* **11**, 9663-9670 (2017).

25. Y. Y. Wen, M. M. Wu, M. Zhang, C. Li, G. Q. Shi, Topological design of ultrastrong and highly conductive graphene films. *Adv. Mater.* **29**, 6 (2017).

26. X. Fang *et al.*, Core-sheath carbon nanostructured fibers for efficient wire-shaped dye-sensitized solar cells. *Adv. Mater.* **26**, 1694-1698 (2014).

27. Y. J. Liu *et al.*, Superb electrically conductive graphene fibers via doping strategy. *Adv. Mater.* **28**, 7941-7947 (2016).

28. S. Yoshiki, S. Masatoshi, Y. Katsuhiro, Relationship between axial compression strength and longitudinal microvoid size for PAN-based carbon fibers. *Carbon* **50**, 2860-2869 (2012).

29. Y. Sugimoto *et al.*, Structure change of carbon fibers during axial compression. *Carbon* **57**, 416-424 (2013).

30. L. Brassart, https://doi.org/10.5281/zenodo.4601590 (2021).

31. M. F. El-Kady, V. Strong, S. Dubin, R. B. Kaner, Laser scribing of high-performance and flexible graphene-based electrochemical capacitors. *Science* **335**, 1326-1330 (2012).

32. W. Gao *et al.*, Direct laser writing of micro-supercapacitors on hydrated graphite oxide

films. *Nat. Nanotechnol.* **6**, 496-500 (2011).

33. P. Kralchevsky, V. Paunov, I. Ivanov, K. Nagayama, Capillary meniscus interaction between colloidal particles attached to a liquid—fluid interface. *J. Colloid Interf. Sci.* **151**, 79-94 (1992).

34. D. Chandra, S. Yang, Capillary-force-induced clustering of micropillar arrays: is it caused by isolated capillary bridges or by the lateral capillary meniscus interaction force? *Langmuir* **25**, 10430-10434 (2009).

35. Y. Huang, J. Wu, K. C. Hwang, Thickness of graphene and single-wall carbon nanotubes. *Phys. Rev. B* **74**, 245413 (2006).

36. P. J. Flory, J. Rehner, Statistical mechanics of cross-linked polymer networks II Swelling. *J. Chem. Phys.* **11**, 521-526 (1943).

37. A. Hüther, X. Xu, G. Maurer, Swelling of n-isopropyl acrylamide hydrogels in water and aqueous solutions of ethanol and acetone. *Fluid Phase Equilibr.* **219**, 231-244 (2004).

38. M. K. Kang, R. Huang, Effect of surface tension on swell-induced surface instability of substrate-confined hydrogel layers. *Soft Matter* **6**, 5736-5742 (2010).

Acknowledgments:

We thank N. Zheng in the State Key Laboratory of Chemical Engineering in Zhejiang University for assistance with performing EDS analysis and SSRF for XRD measurements. **Funding:** This work was funded by the National Key R&D Program of China (grant No. 2016YFA0200200), the National Natural Science Foundation of China (grant No. 52090030, No. 51533008, No. 51703194, No. 11890674, and No. 51873191), Hundred Talents Program of Zhejiang University (grant 188020*194231701/113). **Author contributions:** D.C., Z.L. and C.G. conceived the project. D.C., Z.L. and B.F. designed the experiments. D.C. conducted the experiments. J.L. and Y.L. conducted the finite element analysis and mechanical analysis. L.B. (now at Department of Engineering Science, University of Oxford, Oxford OX1 3PJ, United Kingdom) provided modeling code in finite element analysis. D.C., Z.L., Z.X., B.F. and C.G. analysed the results. D.C., Z.L., B.F. and C.G. wrote the manuscript with input from all authors. C.G. supervised the study. **Competing interests:** The authors declare no competing interests. **Data and materials availability:** All data are available in the manuscript and the supplementary materials.

Supplementary Materials:

Materials and Methods

Supplementary Text

Figs. S1 to S28

Movies S1 to S10

References (*24-38*)

Captions of figures

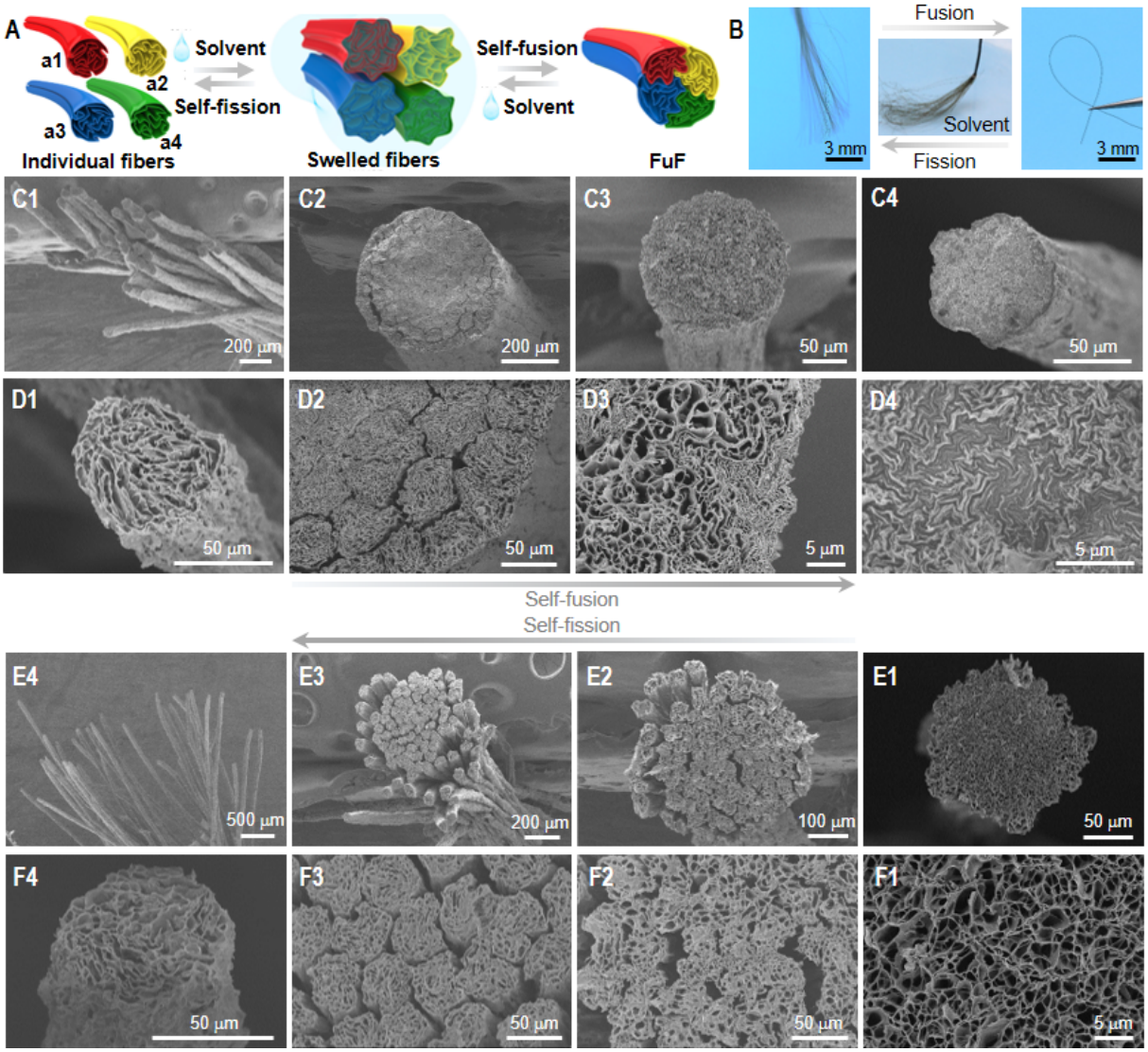

Fig. 1. Reversible fusion and fission of GO fibers. (**A**) Schematic of solvent-triggered reversible self-fusion and self-fission of GO fibers, in which the individual fibers such as a1-a4 are adaptively deformed by solvent-swelling to form a thicker fiber FuF. The dried FuF is swelled in a solvent such as water to gradually fissure into original thinner fibers a1-a4 without exchange of GO sheets among them. (**B**) Photographs of reversible transition between about 100 GO fibers (left) and a single FuF-100 (right), through swelling-assisted (middle) fusion and fission. (**C** to **F**) Sequential SEM images of the water-induced fusion process (from left to right)

of around 100 GO fibers and the reverse fission process (from right to left) of the FuF-100. (D) and (F) show corresponding enlarged local regions in (C) and (E), respectively. (C1) to (C4) and (D1) to (D4) corresponds to 0, 25, 30, and 40 minutes in elapsed time, respectively. (E1) to (E4) and (F1) to (F4) corresponds to 3, 75, 150, and 180 seconds in elapsed time, respectively. The time of fusion is set as zero when the GO fibers in bundle are swelled in water just before being drawn out; so is the fission when the dried FuF-100 is re-soaked in water.

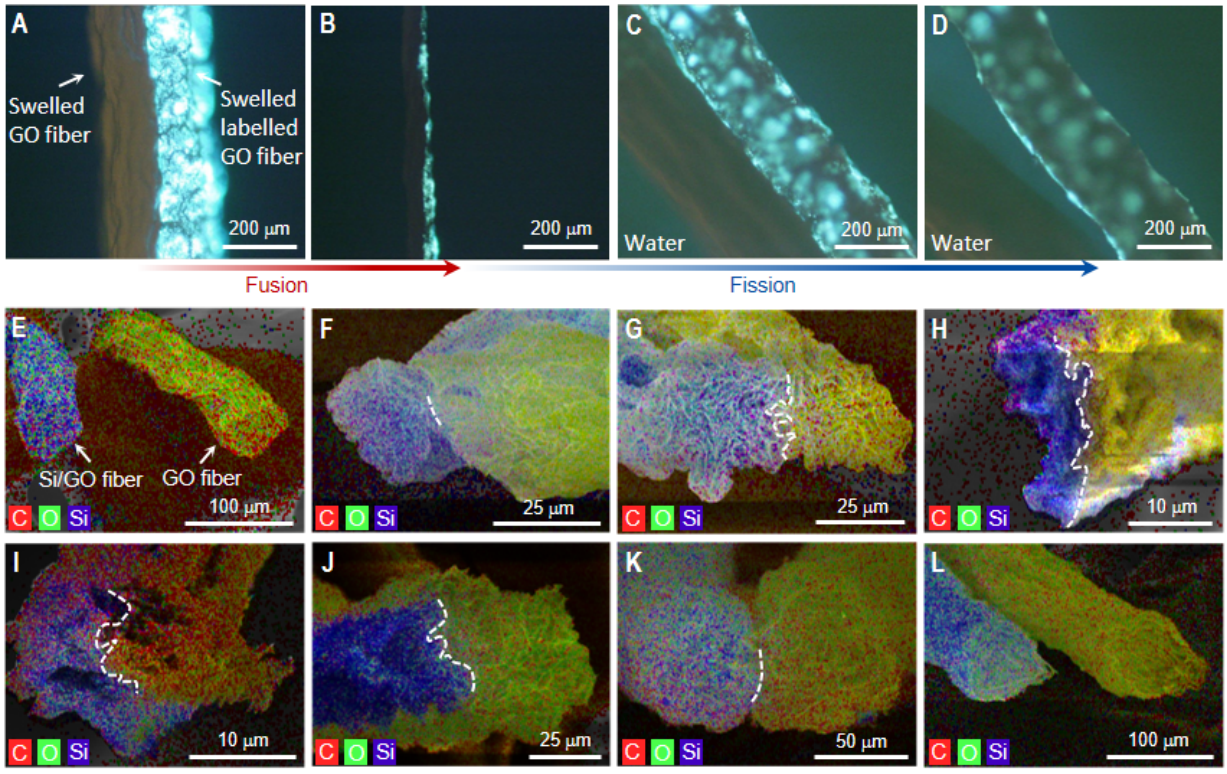

Fig. 2. In-situ fluorescence observation and ex-situ EDS analysis of a fusion-fission cycle. (**A** to **D**) Sequential fluorescent micrographs showing water-triggered fusion (A and B) and fission (B to D) of a neat GO fiber and a fluorescent TPE-Br-labelled GO fiber. A clear interface between the two fibers is distinguished, demonstrating no exchange of GO sheets between them while fusing and fissuring. (**E** to **L**) Sequential overlapped elemental mapping images of carbon (red), oxygen (green) and silicon (blue) elements respectively showing the water-induced fusion (top) and fission (bottom) procedures involving a neat GO fiber and a Si/GO fiber. Dotted lines indicate the interface between the fibers, which suggests interlocking of the synergistically crumpled shells after fusion and corresponding topographical recovery after fission.

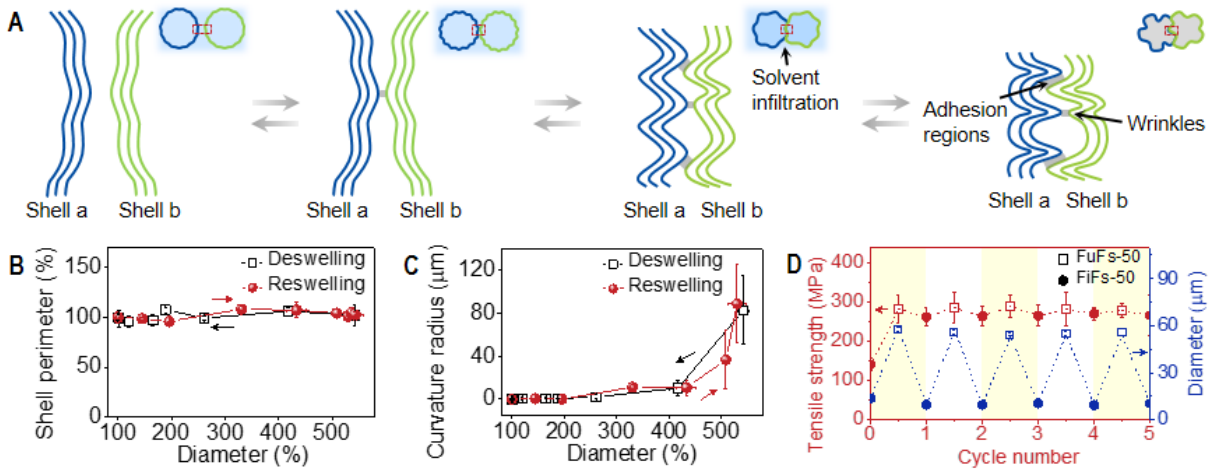

Fig. 3. Dynamic topographical deformation mechanism for reversible fusion and fission. (**A**) Schematic depicting the topographical crumpling of shells at the fiber interface that leads to self-fusion and reversible recovery that induces self-fission. (**B**) Shell perimeter of the water-swelled single GO fibers as a function of fiber diameter during the deswelling and reswelling courses. Corresponding values are plotted relative to that at the initial swelling state. (**C**) Average tip radius of curvature of a unit ripple in different fiber diameter during the deswelling and reswelling procedures of the water-swelled single GO fibers. (**D**) Tensile strength (red) and corresponding diameter (blue) of FuF-50 and FiF-50 as a function of cycle number. The mechanical properties remain constant during several cycles.

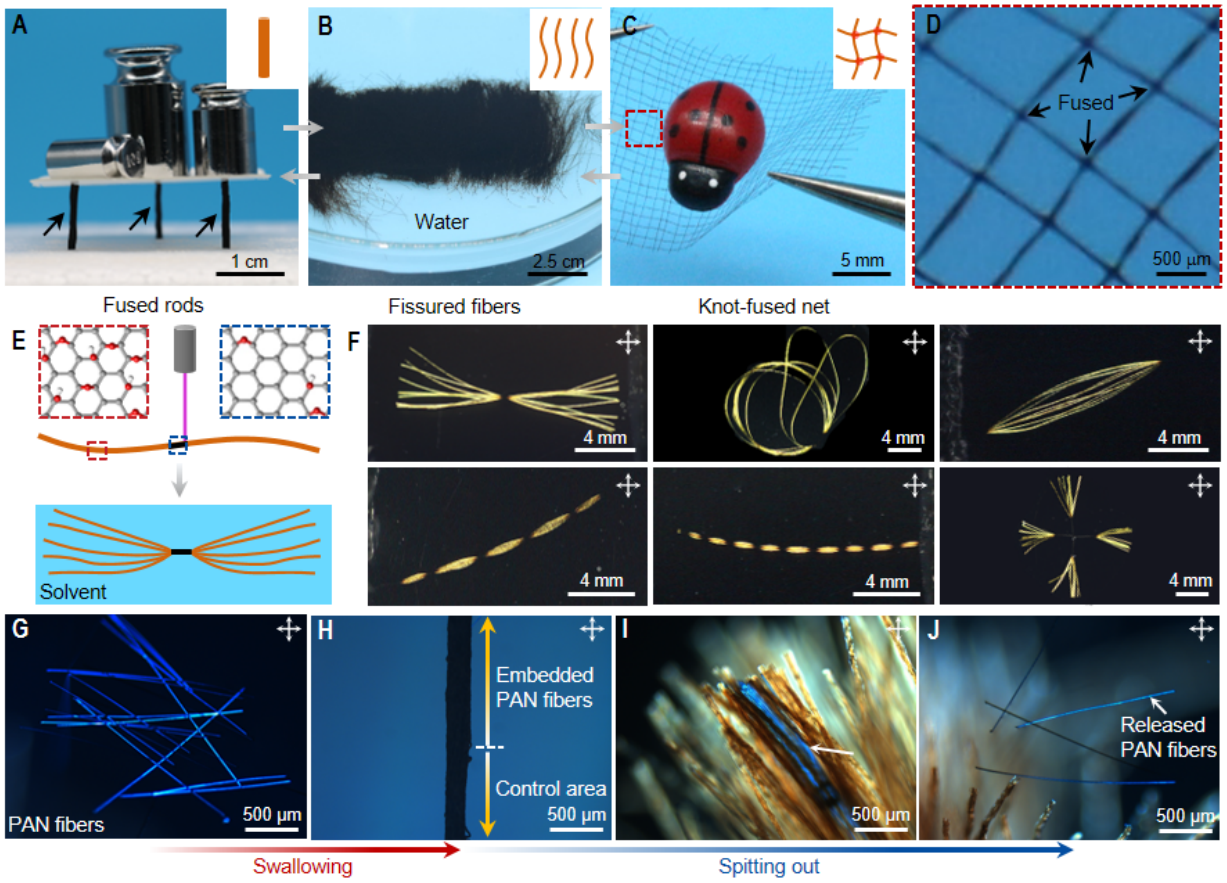

Fig. 4. Reversible fusion-fission promises controllable transforming. (**A** to **D**) Photographs of reversible transitions between a 3D stiff fused GO rod (A) and a 2D flexible knot-fused GO net (C and D) via fission (B) and re-fusion. (**E** and **F**) Illustration and polarized optical photographs showing the programmable 1D and 2D architectures of the locally laser-reduced FuF-10 under water/isopropanol (8:2 v/v) mixture, including star, wristband, multi-block wires with 1, 5 and 9 blocks and dendrite with four arms. (**G** to **J**) Polarized optical microscopy images showing the entrapment of polyacrylonitrile (PAN) staple fibers into a FuF by fusion (G and H) and the reversible expulsion by fission (H to J).